Available online at www.sciencedirect.com
SCIENCE DIRECT®
ELSEVIER
Nuclear Instruments and Methods in Physics Research A 530 (2004) 379–390
NUCLEAR INSTRUMENTS & METHODS IN PHYSICS RESEARCH Section A
www.elsevier.com/locate/nima

MARS14 deep-penetration calculation for the ISIS target station shielding

Noriaki Nakao[a,*], Tomoya Nunomiya[b,1], Hiroshi Iwase[b,2], Takashi Nakamura[b]

[a] *High Energy Accelerator Research Organization (KEK), Oho, Tsukuba, Tanashi Branch, Tsukuba, Ibaraki 305-0801, Japan*
[b] *Cyclotron and Radioisotope Center (CYRIC), Tohoku University, Sendai 980-8578, Japan*

Received 14 November 2003; received in revised form 24 February 2004; accepted 28 February 2004

Available online 22 April 2004

Abstract

The calculation of neutron penetration through a thick shield was performed with a three-dimensional multi-layer technique using the MARS14(02) Monte Carlo code to compare with the experimental shielding data in 1998 at the ISIS spallation neutron source facility of Rutherford Appleton Laboratory. In this calculation, secondary particles from a tantalum target bombarded by 800-MeV protons were transmitted through a bulk shield of approximately 3-m-thick iron and 1-m-thick concrete. To accomplish this deep-penetration calculation, a three-dimensional multi-layer technique and energy cut-off method were used considering a spatial statistical balance. Finally, the energy spectra of neutrons behind the very thick shield could be calculated down to the thermal energy with good statistics, and the calculated results typically agree well within a factor of two with the experimental data over a broad energy range. The $^{12}C(n, 2n)^{11}C$ reaction rates behind the bulk shield were also calculated, which agree with the experimental data typically within 60%. These results are quite impressive in calculation accuracy for deep-penetration problem.

PACS: 24.10.Lx; 28.41.Qb

Keywords: Deep penetration; Shielding experiment; Spallation neutron source; Neutron energy spectra; Monte Carlo

1. Introduction

Although steady progress in computer technologies has made calculations ever faster, reliable calculations of neutron transmission through a very thick shield still remain quite difficult. This is because a long computing time and sophisticated variance reduction techniques are needed to obtain particle fluxes and energy spectra with good statistics. At the same time, the corresponding experimental data for benchmark calculation are rather scarce.

Since 1992, at the ISIS spallation neutron source facility of the Rutherford Appleton Laboratory (RAL) using 800-MeV protons, measurements of deeply penetrating neutrons through a thick bulk shielding were performed to obtain benchmark

*Corresponding author. Tel.: +81-29-879-6004; fax: +81-29-864-4051.

E-mail address: noriaki.nakao@kek.jp (N. Nakao).

[1] Present address: Fuji electric Co. Ltd., Fuji-cho, Hino-shi, Tokyo 191-8502, Japan.

[2] Present address: Gesellschaft für Schwerionenforschung (GSI), Planckstr.1, D-64291, Darmstadt Germany.

0168-9002/$ - see front matter
doi:10.1016/j.nima.2004.02.042

experimental data [1,2]. In a 1998 experiment, concrete and iron shields were additionally installed on the top floor of the target station and the neutron energy spectra and the reaction rates behind shields of various thickness were measured using the activation detectors [3–5]. All of the experimental conditions, the geometry and results are precisely described and are numerically given in Ref. [5].

Since a calculation with three-dimensional geometry based on the actual shield structure could hardly be accomplished, a Monte Carlo calculation under the one-dimensional geometry [6] and a two-dimensional discrete ordinate calculation [7] were performed earlier to analyze this ISIS shielding experiment; they are, however, inadequate to estimate the particle flux distributions. In this work, a deep-penetration calculation using the MARS14(02) Monte Carlo code [8] was performed with a newly developed three-dimensional multilayer technique to analyze the ISIS shielding experiment, and the spatial distribution of the neutron flux and the energy spectra were obtained and were numerically reported in Ref. [9].

2. Experiment

All experimental data which are compared with the calculations in this work are cited from the shielding experiment performed at ISIS in 1998 [3–5]. Neutrons were produced by 800 MeV protons impinging on a thick tantalum target at the center of the target station. The beam intensity was about 170 μA at the target with a 50-Hz repetition rate.

A cross-sectional view of the target station at ISIS is shown in Fig. 1. The target vessel is covered with a shielding plug consisting of 284-cm-thick steel (density of 7.35 g/cm^3) and 97-cm-thick concrete (density of 2.3 g/cm^3), a 6-cm-thick steel vacuum plate and a steel-support plate. The surface of the support plate was located 528 cm above the beam line as shown in Fig. 2. A duct (42.5 × 42.5 cm^2 cross-section) through the bulk shield, which supplies helium gas to the target vessel, reaches the top of the target station down stream as shown in Fig. 1.

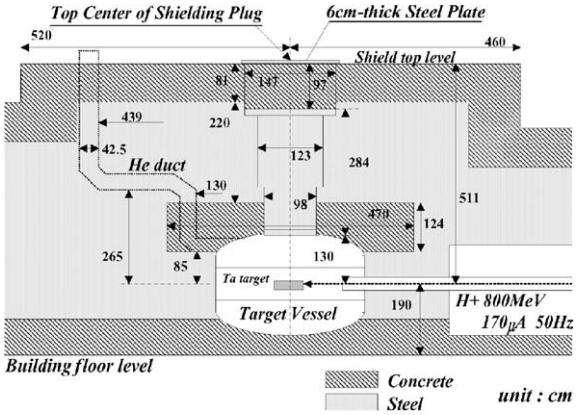

Fig. 1. Cross-sectional view of the target station of neutron spallation source with an 800-MeV proton beam at ISIS.

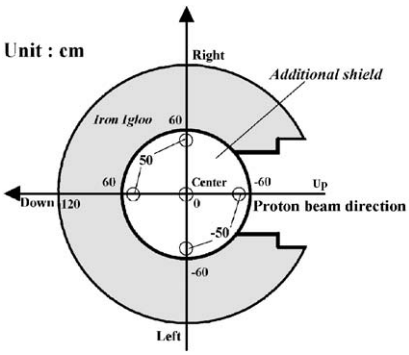

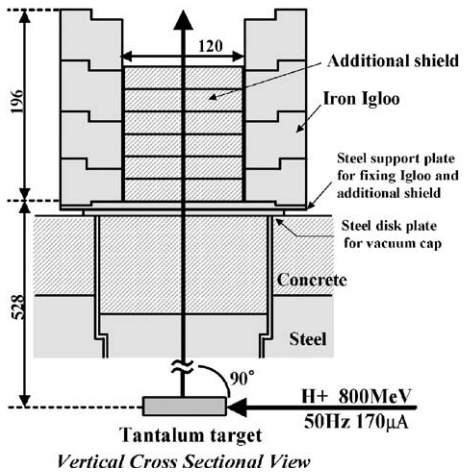

Fig. 2. Horizontal and vertical cross-sectional views of the iron-igloo and an additional shield. The five detector positions of "center", "up50", "down50", "left50" and "right50" are shown as white circles in the upper figure.

In the experiment of 1998, an iron igloo was equipped on the top of the target station for reduction of the background neutrons mainly due to the spurious neutrons leaked through the He duct. Additional shields of 119-cm diameter by 20–120-cm-thick concrete (density of 2.36 g/cm^3) and 10–60-cm-thick iron (density of 7.8 g/cm^3) were assembled on the support plate inside the iron igloo, as shown in Fig. 2, in order to measure the attenuation profiles of the neutron flux through the additional shields.

Neutrons behind various thicknesses of the additional concrete or iron shield were measured using activation detectors of graphite, bismuth and aluminum. The graphite activation detectors were set at various positions called "center", "up", "down", "left" and "right" on an additional shield surface of each thickness, as shown in Fig. 2. The other detectors were set only at the center position. Neutron reaction rates of $^{12}C(n,2n)^{11}C$, $^{27}Al(n,\alpha)^{24}Na$ and $^{209}Bi(n,xn)^{210-x}Bi$ $(x=4-10)$ were obtained, and their attenuation profiles through concrete and iron were clarified. Attenuation lengths of high-energy neutrons for concrete and iron were also estimated in this experiment. A multi-moderator spectrometer (Bonner ball) using indium-oxide activation detectors [10] was also used for the measurement, and the neutron energy spectra in the energy range from thermal to 400 MeV were obtained by an unfolding technique of the SAND-2 code [11] using the above reaction rates (C, Al and Bi) and $^{115}In(n,\gamma)^{116m}In$. The response functions of the indium Bonner ball were cited from Ref. [10], and the reaction cross-sections of $^{12}C(n,2n)^{11}C$ were evaluated by eye from the experimental data [12,13], those of $^{27}Al(n,\alpha)^{24}Na$ calculated by Fukahori using the ALICE code [14], and those of $^{209}Bi(n,xn)^{210-x}Bi$ cited from the ENDF/B-VI high-energy library [15].

3. Calculation geometry

Fig. 3 shows the calculational model of the target system, which consists of target ($Ta+D_2O$ cooling water), container ($Fe+D_2O$), and reflector ($Be+D_2O$). All of these are of cylindrical

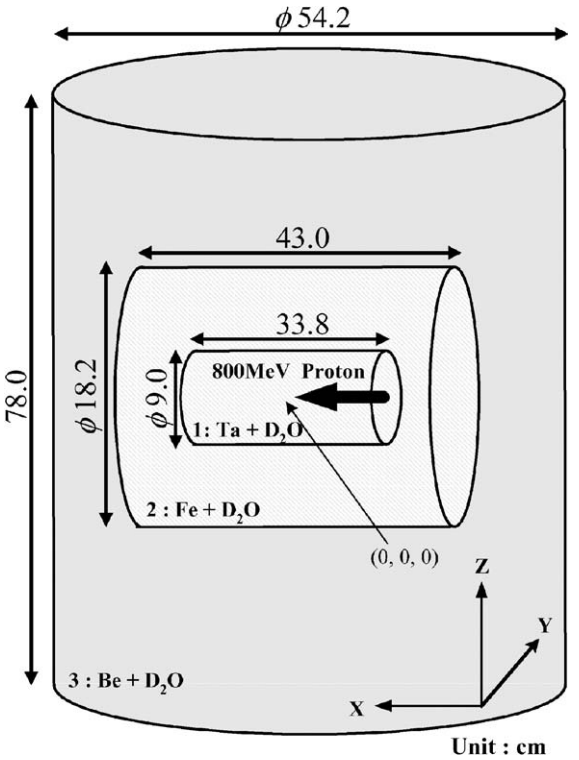

Fig. 3. Geometry of target system consisting of a target, a container and a reflector. All cylinders have a common center at (0, 0, 0).

shape and have a common center. Two small cylinders are parallel to the X-axis which is the proton beam direction, and the largest cylinder is perpendicular to it.

For calculations, the actual shield geometries shown in Figs. 1 and 2 were simplified, and the calculational geometries used in this study in vertical cross-section are shown in Figs. 4 and 5 for the Y–Z plane and the X–Z plane, respectively. Horizontal cross-sections are exemplified in Figs. 6(a), (b) and (c) at the horizontal levels of A, B and K in Fig. 5, respectively. The He-duct was also taken into account through the bulk shield geometry.

The densities and atomic compositions of the target system and the shields are given in Tables 1 and 2, respectively, and the heterogeneous structure was changed homogeneously. As the deuteron is not included in the MARS code, hydrogen was used instead of the deuteron, and the atomic

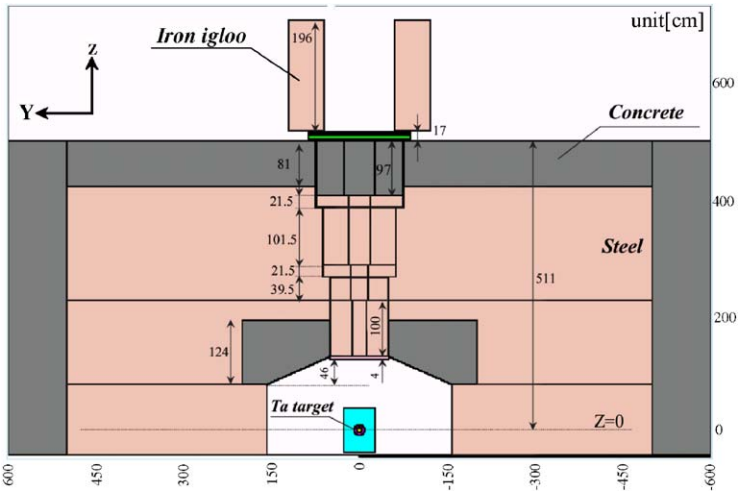

Fig. 4. Cross-sectional view of the Y–Z plane of the simplified geometry of target station used in the calculation.

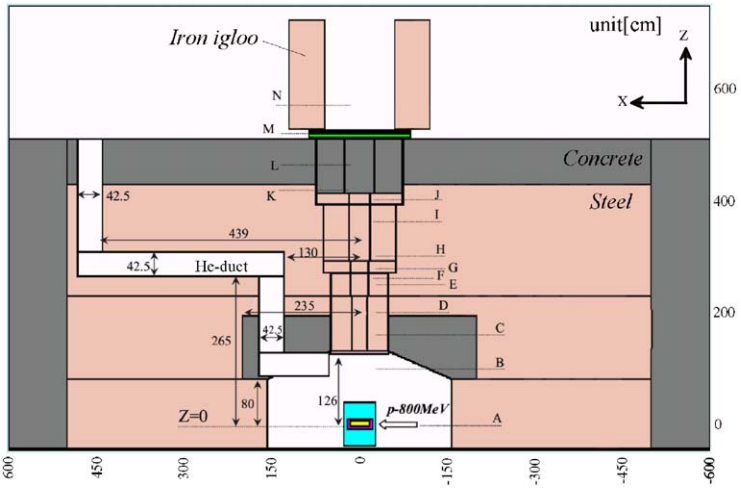

Fig. 5. Cross-sectional view of the X–Z plane of the simplified geometry of target station used in the calculation.

densities for hydrogen were set to be equivalent to that of the deuteron. The composition of the iron-igloo was considered to be the same as that of the additional iron shield.

4. Calculational methods

4.1. Secondary particles from the target system

An 800-MeV proton beam was injected onto the bottom center of the smallest cylinder (target) along the X-axis, as shown in Fig. 3. The energies, coordinates, directions and weights of the neutrons, protons and pions leaked from the target system were first calculated with the MARS14(02) Monte Carlo code and stored as source particles for a bulk shield calculation. Since the geometry of the target system was symmetrical with respect to the $Z = 0$ plane and the bulk shield of $Z<0$ was not taken into account in this work, particles leaked in the region of $Z<0$ were stored as those having an absolute value of the Z-coordinate but with the Z vector reversed, and the weights

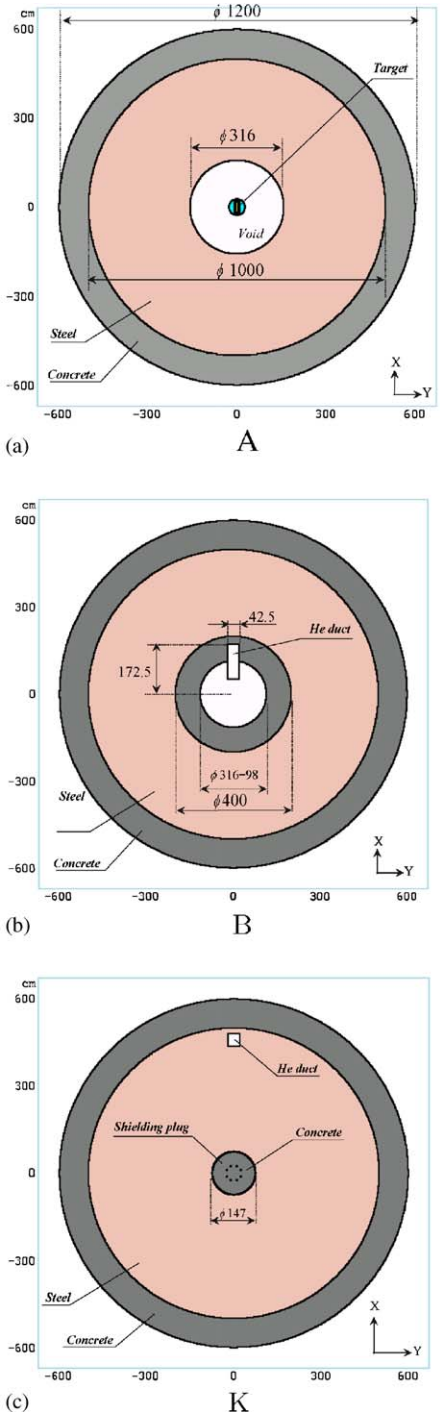

Fig. 6. Horizontal cross-sectional views of the X–Y plane at A, B and K cross-sections of Fig. 5.

of all particles were multiplied by 0.5, as shown in Fig. 7.

4.2. Three-dimensional multi-layer calculation for variance reduction

To accomplish a deep-penetration calculation with good statistics in a reasonable computing time, a three-dimensional multi-layer technique was newly developed in this work. The shielding geometry was three-dimensionally divided into several layers, as shown in Fig. 8, where layer (a) is the target system, layer (b) is the target vessel, and layers (c)–(h) are the bulk shield, layer (i) is the uppermost bulk shield and the upper space, and layer (j) is the area surrounded with the iron-igloo. If a particle crossed outwards from a layer boundary, the particle tracking was terminated and the particle informations were recorded in a file. They were then used for a next-layer calculation as source particles having the numbers multiplied by a factor of 5–10, like a splitting method. The initial weight of the particle in the new layer, W_2, is given as

$$W_2 = \frac{N_{1\_\mathrm{leak}}}{N_1} W_1 \tag{1}$$

where W_1 is the weight of the particle leaked from the previous layer, N_1 is the number of source particles in the previous layer and N_{1_leak} is the number of particles leaked from the previous layer. Track-length estimators (e.g. 20-cm-diameter and 2-cm-thick) were located at various positions throughout the bulk shield and above the shield top to obtain the neutron energy spectra.

In the final layer (j) of Fig. 8, three calculations were carried out by changing the additional shield (air, concrete and iron) using the same source particles leaked from layer (i). The source particles were emitted from the shield top floor ($Z =$ 511 cm) and from the outer surface of the iron-igloo shown in Fig. 8.

4.3. Statistical balance

Since the forwardness of the particle production at the target and the streaming through the large

Table 1
Atomic compositions and averaged densities of the target system and the surrounding materials used in this calculation

Averaged density	Targets 14.5 g/cm^3		Containers 3.58 g/cm^3		Reflectors 1.69 g/cm^3	
	wt%	Atom/cm^3	wt%	Atom/cm^3	wt%	Atom/cm^3
H[a]	0.19	8.29E+21[b]	3.9	4.22E+22	21.1	1.37E+22
Be	—	—	—	—	68.3	9.83E+22
O	0.75	4.14E+21	15.6	2.11E+22	10.6	6.84E+21
Fe	—	—	80.5	3.10E+22	—	—
Ta	99.06	4.84E+22	—	—	—	—

[a] Deuteron is replaced by hydrogen.
[b] Read as 8.29×10^{21}.

Table 2
Atomic compositions of the bulk shield and the additional shields used in this calculation

		Concrete		Iron	
Bulk shield					
	Density:	2.3 g/cm^3		7.35 g/cm^3	
Additional shield					
	Density:	2.36 g/cm^3		7.8 g/cm^3	
		wt%	Atom/cm^3	wt%	Atom/cm^3
H		1.08	1.52E+22[a]	—	—
C		6.01	7.11E+21	0.14	5.47E+20
O		51.34	4.56E+22	—	—
Na		0.12	7.42E+19	—	—
Mg		0.28	1.64E+20	—	—
Al		0.76	4.00E+20	—	—
Si		12.56	6.35E+21	0.32	5.35E+20
P		—	—	0.02	3.03E+19
S		0.19	8.42E+19	0.008	1.34E+19
K		0.28	1.02E+20	—	—
Ca		21.99	7.79E+21	—	—
Ti		0.03	8.90E+18	—	—
Mn		—	—	1.0	8.55E+20
Fe		5.36	1.36E+21	98.51	8.28E+22

The composition of the iron-igloo is equivalent to that of the additional shield.
[a] Read as 1.52×10^{22}.

He-duct are dominant as seen in Fig. 1, the particle intensity downstream is much higher than in the other areas. To keep a good statistical balance in the whole region of a layer, particles leaked around the He-duct were recorded separately at downstream (“forward-duct”), at side, and at upstream (“side-back”), in the case of the layer (b) (see Fig. 8), as shown in Fig. 9. Using these two separate sources, the calculations from the layer (c) to the layer (i) (see Fig. 8) were performed in two ways, and the two results were summed up at every estimator. A simple flow chart of this step-by-step calculation is shown in Fig. 10. Note that each layer includes the previous two layers (e.g. layer (c) includes layer (a) and layer (b)) to take the reflected particles into consideration. The thicknesses of the layers were from 100 to 200 cm.

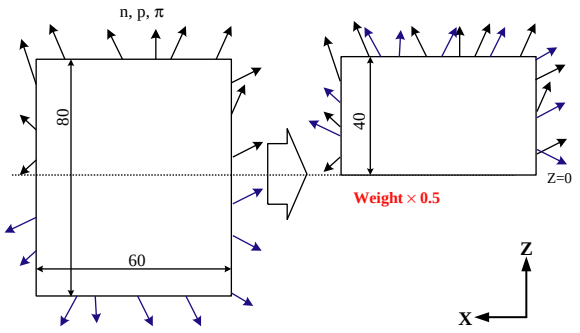

Fig. 7. Schematic view of the target system calculation (layer (a) in Fig. 8).

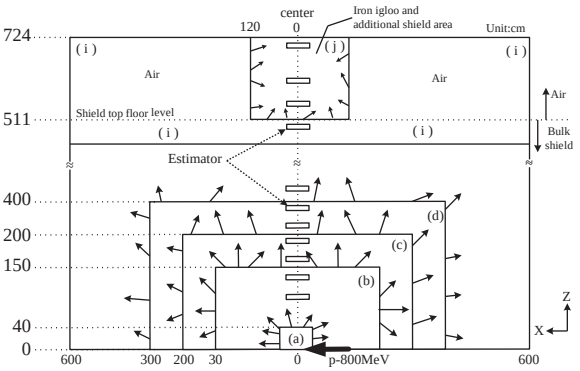

Fig. 8. Schematic view of the three-dimensional multi-layer calculation. Protons, neutrons and pions crossing outwards the layer boundaries are stored in a file with their energy, coordinates, directions and weight to be used as a source in the next layer calculation.

4.4. Energy cut-off

Since the experimental data are given above the shield top floor, in order to save computing time, the cut-off energies of all particles were set to 20 MeV, up to about 1 m below the shield top floor ($Z = 394$ cm); above that region, the cut-off energies of neutrons and charged hadrons were set to be thermal and 0.2 MeV, respectively. This approximation can be supported by the following consideration. The neutron attenuation in the lower energy region is much faster than that in the high-energy region, and the contribution of the lower energy neutron penetration through the 1-m-thick shield is negligible compared with the lower energy neutrons generated newly from the high-energy hadron cascade. For a calculation below 14.5 MeV, the MARS default option of the 28-group-BNAB low-energy neutron transport [16] was used in this study.

4.5. Data analysis

The neutron energy spectra were estimated by a track-length estimation method. The reaction rates of activation detectors were estimated using the calculated neutron energy spectra and cross-section data mentioned in Section 2. The neutron dose rate is estimated using the calculated neutron energy spectra and the neutron flux-to-dose conversion factor of 1-cm depth cited from ICRP pub.74 [17]; it is assumed to be constant at $E >$ 200 MeV.

5. Results and discussions

5.1. Secondary particles from the target system

Fig. 11 shows the angular- and energy-distributions of the neutrons above 20 MeV (per lethargy, per sr and per proton) leaked from the target system. It can be seen that the neutrons generated in the forward direction reach 800 MeV which is the energy of the primary proton beam, and the energy spectrum becomes much softer with the emission angle. The leakage ratios of protons and pions to that of neutrons are about 10% and 0.1% from the calculation results.

5.2. Neutron energy spectra

Fig. 12 shows the calculated neutron energy spectra through the bulk shield up to the shield top floor at the center position (see Fig. 2). All neutron energy spectra have a hadron cascade peak at around 100 MeV. The neutron energy spectrum in a concrete region at $Z = 422.5$ cm has a typical $1/E$ slowing-down spectrum (flat in lethargy spectrum). On the shield top floor inside the iron-igloo shown at $Z = 528.6$ cm in Fig. 12, the neutron spectrum has a broad peak at around a few hundred keV over the region from 10^{-4} to

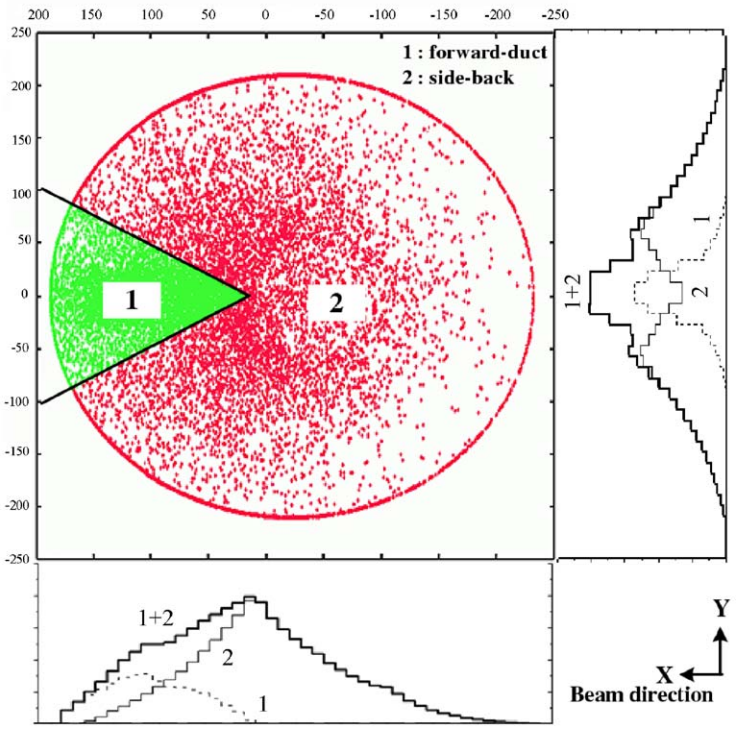

Fig. 9. Graphical plots of recorded neutrons leaked at layer (b) calculation. Calculation of layer (c) is carried out separately by using two different sources of (1) "forward-duct" and (2) "side-back".

10 MeV due to inelastic scattering in the iron plates.

Fig. 13 shows the calculated neutron energy spectra on the shield top floor, behind the 60-cm-thick additional concrete and behind the 30-cm-thick additional iron at the "center" position compared with the experimental data [5]. High-energy neutrons above 250 MeV are not counted in the calculations. Note that the calculated energy spectrum on the additional concrete shield is in remarkably good agreement with the experiment within about 40% in the energy region above 1 MeV. Generally, the calculated energy spectra agree with the measured ones within a factor of 2 over a broad energy range with the maximum differences reaching a factor of 3–6, mainly in the thermal energy region, where the BNAB cross-section data compiled in the MARS code have poor accuracy. These results are quite impressive in the transport calculation through such a very thick shield, where the neutron flux attenuation reaches seven orders of magnitude, 10^{-7}, as shown later in Fig. 14, while on the other hand, the previous calculation with the ANISN and HETC code [6] underestimated about one order of magnitude.

It is said that the calculation using the MCNP option instead of the 28-group-BNAB of MARS for the low-energy neutron transport is expected to improve the agreement with the experiment below 14.5 MeV.

5.3. Attenuation of the reaction rates

Attenuation profile of the $^{12}C(n, 2n)^{11}C$ reaction rates through the bulk shield and above the shield top floor at the center position which were estimated from the calculated energy spectra were obtained with good statistics, as shown in Fig. 14. Since the $^{12}C(n, 2n)^{11}C$ reaction has a threshold energy of 20 MeV and the reaction cross-section above 20 MeV has almost a constant value of 20 mb, the $^{12}C(n, 2n)^{11}C$ reaction rate corresponds to the high-energy neutron flux above 20 MeV.

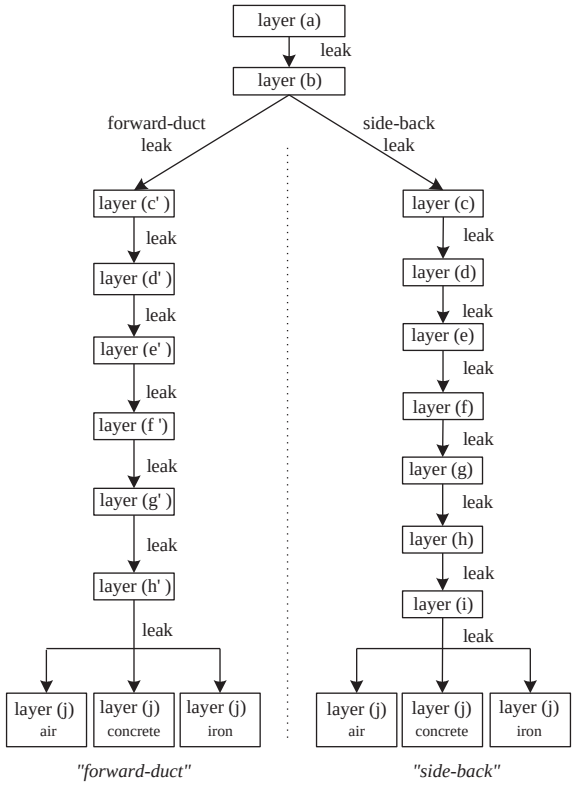

Fig. 10. Flow chart of a step-by-step calculation. Right-lane indicates "side-back" calculation and left-lane indicates "forward-duct" calculation. Three calculations were carried out using same source particles leaked from layer (i) at "side-back" and those from layer (h') at "forward-duct", respectively.

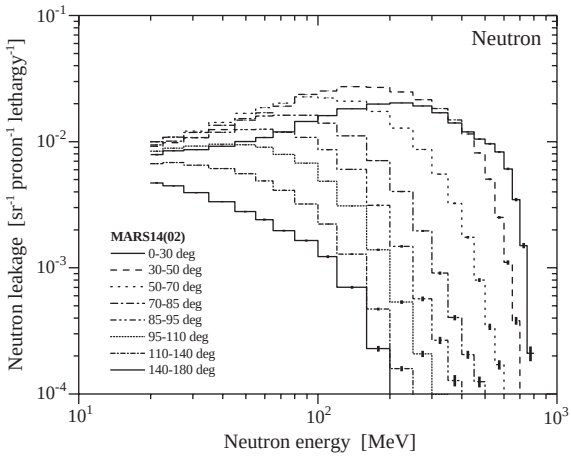

Fig. 11. Angular and energy distributions of neutrons leaked from the target assembly surface calculated with the MARS14 Monte Carlo code.

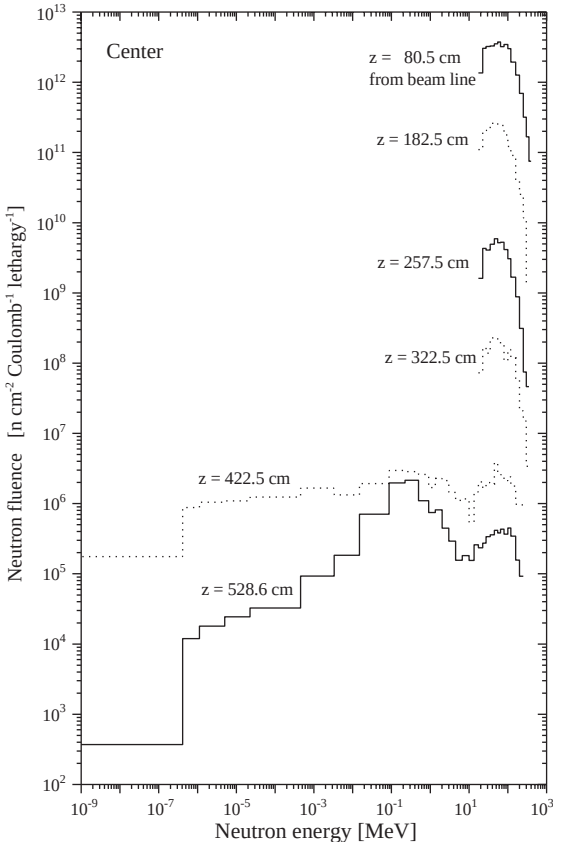

Fig. 12. Calculated neutron energy spectra in the bulk shield and above the shield top center.

Therefore, Fig. 14 gives the high-energy neutron flux attenuations through iron and concrete. As previously described, the high-energy neutron flux decreases about seven orders of magnitude, 10^{-7} from the target position up to the shield top floor.

Fig. 15, which is the expansion in the region above the shield top area of Fig. 14, shows the attenuation profiles of the $^{12}C(n,2n)^{11}C$ reaction rates above the shield top floor without an additional shield (e.g. air), behind the additional concrete and iron shields at the "center" position (see also Table 3). The attenuation profiles of the measured and calculated reaction rates show a slight difference especially in the case of air, and the discrepancy of the reaction rate is typically within 60% and within a factor of 2 in the maximum case. It should be clarified that this calculation gives more accurate values than the

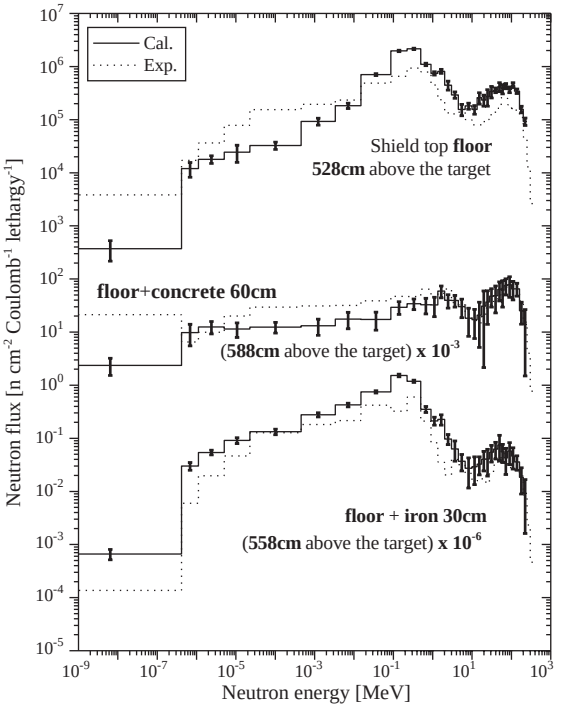

Fig. 13. Comparison between the calculated and measured neutron energy spectra on the shield top floor, behind the additional concrete and iron shields at "center" position.

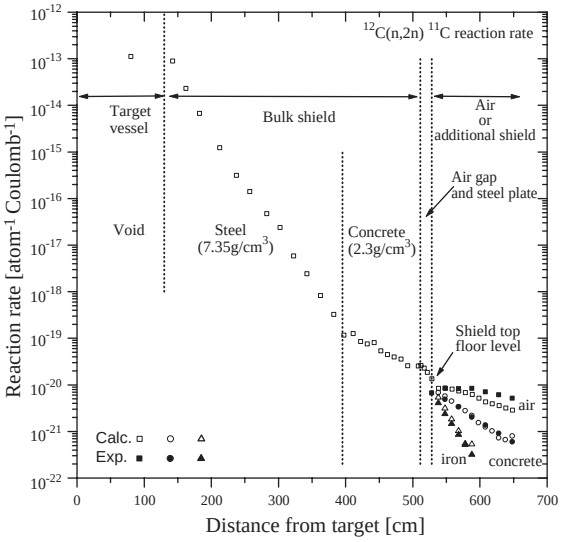

Fig. 14. Calculated attenuations of $^{12}C(n,2n)^{11}C$ reaction rate through the bulk shield, compared with the measured data above the shield top at the "center" position.

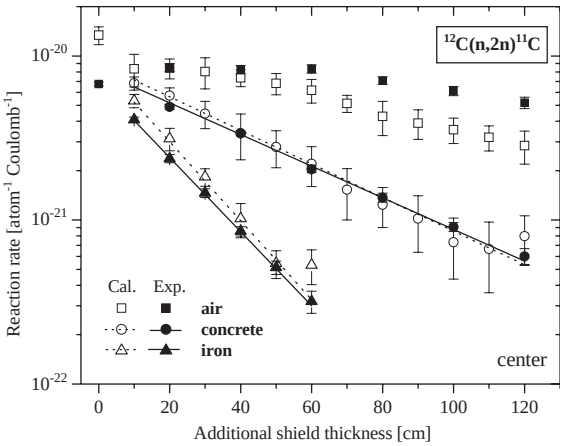

Fig. 15. Comparison between the calculated and measured attenuations of $^{12}C(n,2n)^{11}C$ reaction rate above the shield top (air) and behind the additional concrete and iron shields at the "center" position.

earlier simple calculations [6], which gave underestimations of about one order of magnitude.

Figs. 16 and 17 show the spatial distributions of the estimated $^{12}C(n,2n)^{11}C$ reaction rates in the inner area of the igloo on the shield top, along the up-down direction (X-axis) behind the additional concrete and iron shields, respectively. The calculated data are compared with the experimental results and agree well within about a factor of 2. Both calculated and experimental results give increasing trend of the reaction rates toward downstream due to the contribution of neutron leakage through a large He-duct as described before.

5.4. Neutron attenuation length

The neutron attenuation lengths were estimated from the attenuation profiles of the $^{12}C(n,2n)^{11}C$ reaction rates using the least-mean square method, which corresponds to the neutron flux attenuation above 20 MeV. Attenuation curves based on the attenuation lengths are drawn as straight lines in Fig. 15. The attenuation lengths for both concrete and iron, estimated from the calculated $^{12}C(n,2n)^{11}C$ reaction rates, are about 7% shorter than those estimated from the experiment, as given in Table 3.

Table 3
Comparison of the measured and calculated attenuation lengths estimated from the $^{12}C(n,2n)^{11}C$ reaction rate at "center" position

Shielding material	Attenuation length (g/cm^2)		
	Exp.	Cal.	C/E
Concrete (2.36 g/cm^3)	125.4±5.1	116.7±3.8	0.93
Iron (7.8 g/cm^3)	161.1±2.1	150.3±5.8	0.93

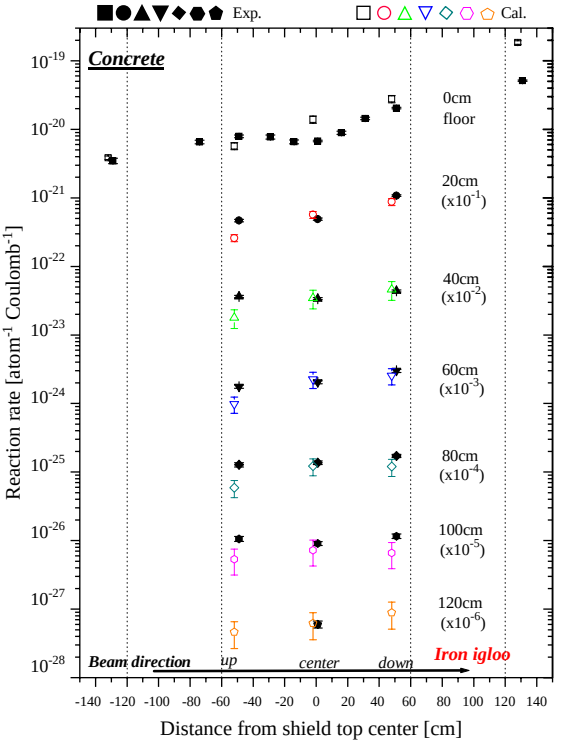

Fig. 16. Comparison between the calculated and measured $^{12}C(n,2n)^{11}C$ reaction rates above the shield top behind the additional concrete shield along the up-down axis (X-axis).

6. Conclusion

A deep-penetration calculation was performed with a three-dimensional multi-layer technique using the MARS14(02) Monte Carlo code. The neutron energy spectra behind a very thick shield of approximately 3-m-thick iron and 1-m-thick concrete were calculated with good statistics in the energy range from thermal to 400 MeV. The calculated results were compared with the ISIS shielding experiment performed in 1998, and the neutron energy spectra typically agreed within a factor of 2 over a broad energy range, with the maximum differences reaching a factor of 6 mainly in the thermal energy region. The $^{12}C(n,2n)^{11}C$ reaction rates were also estimated from the calculated neutron energy spectra, and typically agreed with the experiment within 60%, in the maximum case within a factor of 2 behind the additional concrete and iron shields at the "center". These results are quite impressive in the calculation for deep-penetration problems.

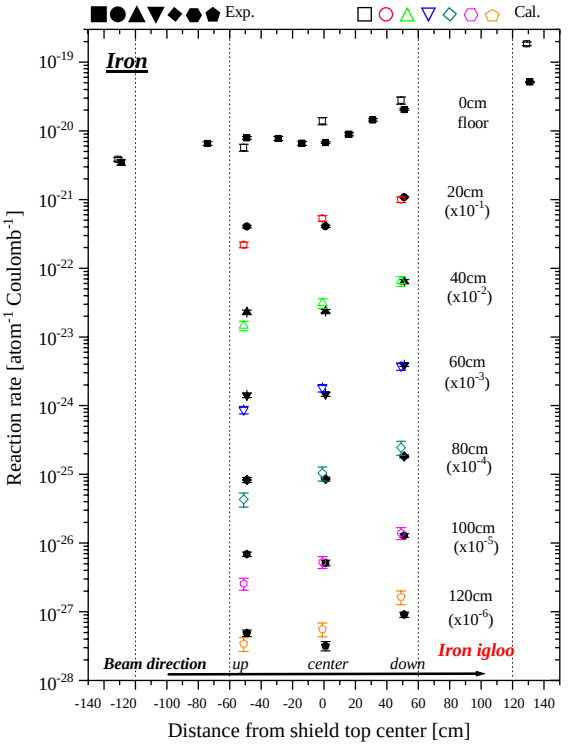

Fig. 17. Comparison between the calculated and measured $^{12}C(n,2n)^{11}C$ reaction rates above the shield top behind the additional iron shield along the up-down axis (X-axis).

Acknowledgements

We would like to thank Dr. Nikolai Mokhov of Fermi National Accelerator Laboratory for his

great help and advice to this work using the MARS code system.

References

[1] Y. Uwamino, T. Shibata, T. Ohkubo, S. Sato, D. Perry, Study on bulk shielding of an 800-MeV proton accelerator, OECD/NEA/NSC, The Specialists' Meeting on Shielding Aspects of Accelerators, Targets, and Irradiation Facilities (SATIF-1), Arlington, TX, April, 1994, p. 185.

[2] N. Nakao, T. Shibata, T. Ohkubo, S. Sato, Y. Uwamino, Y. Sakamoto, D.R. Perry, Shielding experiment at 800 MeV proton accelerator facility, Proceedings of the 1998 ANS Radiation Protection and Shielding Division Topical Conference, Vol. 2, 1998, Nashville, TN, pp. 192–199.

[3] T. Nunomiya, N. Nakao, P. Wright, T. Nakamura, E. Kim, T. Kurosawa, S. Taniguchi, M. Sasaki, H. Iwase, T. Shibata, Y. Uwamino, S. Ito, D.R. Perry, Nucl. Instr. and Meth. B 179 (2001) 89.

[4] N. Nakao, T. Shibata, T.Nunomiya, T. Nakamura, E. Kim, T. Kurosawa, S. Taniguchi, M. Sasaki, H. Iwase, Y. Uwamino, S. Ito, P. Wright, D.R. Perry, Deep penetration experiment at ISIS, OECD/Nuclear Energy Agency, The Specialists' Meeting on Shielding Aspects of Accelerators, Targets and Irradiation Facilities (SATIF-5), Paris, France, 2000, p. 18.

[5] T. Nunomiya, N. Nakao, P. Wright, T. Nakamura, E. Kim, T. Kurosawa, S. Taniguchi, M. Sasaki, H. Iwase, T. Shibata, Y. Uwamino, S. Ito, D.R. Perry, Experimental data of deep-penetration neutrons through a concrete and iron shield at the ISIS spallation neutron source facility using an 800-MeV proton beam, KEK Report 2001-24, February 2002.

[6] N. Nakao, Y. Uwamino, Deep penetration calculation compared with the shielding experiments at ISIS, Proceedings of Ninth International Conference on Radiation Shielding, J. Nucl. Sci. Technol. (Suppl. 1) (2000) 162.

[7] H. Handa, M. Saitoh, K. Hayashi, K. Yamada, T. Abe, Y. Uwamino, Analysis on high energy neutron shielding experiments in ISIS, SARE-3, KEK Proceedings 97-5, Vol. 97-5, 1997, p. 300.

[8] N.V. Mokhov, The Mars Code System User's Guide, Fermilab-FN-628 (1995); N.V. Mokhov, O.E. Krivosheev, MARS Code Status, Fermilab-Conf-00/181 (2000); http://www-ap.fnal.gov/MARS.

[9] T. Nunomiya, N. Nakao, H. Iwase, T. Nakamura, Deep-penetration calculation for the ISIS target station shielding using the MARS Monte Carlo code, KEK Report 2002-12, March 2003.

[10] Y. Uwamino, T. Nakamura, A. Hara, Nucl. Instr. and Meth. A 239 (1985) 299.

[11] W.N. McElroy, S. Berg, T. Crockett, R.G. Hawkins, A computer automated interactive method for neutron flux spectra determination by foil activation, AFWL-TR-67-41, Air Force Weapons Laboratory, Kirtland Air Force Base, 1967.

[12] E. Kim, T. Nakamura, A. Konno, Nucl. Sci. Eng. 129 (1998) 209.

[13] Y. Uno, Y. Uwamino, T.S. Soewarsono, T. Nakamura, Nucl. Sci. Eng. 122 (1996) 247.

[14] M. Blann, Code ALICE/89, 1989.

[15] Evaluated Nuclear Data File, ENDF/B-VI, National Neutron Cross Section Center, Brookhaven National Laboratory, 1990.

[16] L.P. Abagyan, N.O. Bazazyants, M.N. Nikolaev, A.M. Tsybulya, Group Cross-Sections for Reactor and Shielding Calculations, Energoizdat, Moscaw, 1981.

[17] International Commission on Radiological Protection, Conversion Coefficients for Use in Radiological Protection against External Radiation, ICRP Publication 74, Annals of the ICRP, Vol. 26, No. 3/4, Pergamon, Oxford, 1996.